Precision Engineering 56 (2019) 412–421

Contents lists available at ScienceDirect

Precision Engineering

journal homepage: www.elsevier.com/locate/precision

Molecular dynamics study of direct localized overpotential deposition for nanoscale electrochemical additive manufacturing process

Anne Brant, Murali Sundaram*

Department of Mechanical and Materials Engineering, University of Cincinnati, Cincinnati, OH, 45220, USA

ARTICLE INFO

Keywords:
Additive manufacturing
Electrochemical processes
Electrodeposition
LAMMPS
Molecular dynamics simulation
Nanomanufacturing

ABSTRACT

A quasi-deterministic molecular dynamics simulation was performed to study the migration and deposition of ions under the influence of charged, constant-potential electrodes. The input parameters that were varied include tool size, tool potential, substrate potential, interelectrode gap, and concentration. The output parameters of the deposit that were monitored included deposition height over time, number of atoms deposited over time, averaged current density, and deposition quality. Variation of the interelectrode gap or concentration resulted in changes to the deposition rate and quality that were inversely related to each other. It was found that there is an optimal radius to simultaneously maximize deposition speed and quality. An increase in the voltage difference between the tool and substrate improved the rate and overall quality of the deposition, but the highest voltage differences between the electrodes led to a hollow region in the center of the deposit due to ion depletion. Low concentration similarly led to ion depletion conditions. A low amount of anode-cation interactions due to a small tool or low concentration resulted in a deposit that engulfed the tool due to less overall electrostatic interactions repelling the cations from the tool. It was found that an increased output current density did not necessarily coincide with increased output deposit quality.

1. Introduction

Additive manufacturing (AM) is a versatile approach to manufacturing that allows for complex parts to be constructed directly from computer designs. AM encompasses a wide variety of processes that use different mechanisms of material addition. Electrochemical additive manufacturing (ECAM) is an emerging, non-traditional AM process that extends the localized electrodeposition of metal [1] into a method of additive manufacturing of complex three-dimensional parts [2]. The ECAM process holds many unique advantages that distinguish it from conventional AM processes, including its non-thermal nature, independence from adhesives and support structures, direct feedback monitoring, ease of material supply, and flexibility across different size scales and work materials [2,3]. While miniaturization in additive manufacturing is in demand across many industries, including consumer, electronics, medical, automotive, and aerospace; the features created by the localized electrodeposition process have been cited to be of particular interest for actuators and sensors, communication devices, integrated circuits, thermodynamic and hydrodynamic devices, and surgical robots [4,5].

A significant amount of conventional additive manufacturing processes rely on heat to melt the starting material, sinter powders together, or vaporize a binder [6]. This approach leads to unwanted thermal defects, which cause deviations in output geometry, material properties, chemical composition, and part performance [7,8]. Because electrodeposition can be performed at room temperature, ECAM can be operated as a nonthermal process and entirely avoid these complications.

Even non-thermal AM processes, such as adhesive-based binder jetting or sheet lamination, are plagued by limitations in output part integrity. Their reliance on coarse work materials and adhesives leads to inhomogeneous parts, with material properties, surface quality, and resolution limited to that of the constituent materials. The handling and application of adhesives and binders also introduces complications [9–12]. Unlike these processes, ECAM directly generates metallurgical bonds through atom-by-atom deposition, and material is directly supplied via the surrounding electrolyte.

Support structures are another issue inherent to many additive manufacturing processes, which introduce disadvantages due to build time, material waste, labor, and risk of part damage. The electrochemical nature of material addition in ECAM allows for support structures to be avoided entirely. The feasibility of programming ECAM tool paths to achieve increased complexity in deposit geometry without relying on support structures was demonstrated elsewhere [13].

---

* Corresponding author.
E-mail address: murali.sundaram@uc.edu (M. Sundaram).

https://doi.org/10.1016/j.precisioneng.2019.01.010
Received 25 September 2018; Received in revised form 18 December 2018; Accepted 18 January 2019

Finally, highly unique advantages of ECAM that are not seen in many conventional processes include versatility across size scales and direct feedback on the mechanism of the part build. Conventional AM methods typically work at a limited size scale, and may rely on secondary feedback such as optical or thermal imaging, which may be limited to certain size scales and involve processing of large amounts of information. In contrast, because ECAM is an electrochemical process, the size scale may be varied across the macro, micro, and nano regimes by a change in tool size. At any size scale, the very current that causes material addition can be rapidly monitored, captured, and used for control.

Advancing the Nano ECAM process to become a predictable, reliable, and commercially-viable additive manufacturing process requires a deep understanding of how the electrical and chemical phenomena are linked in the act of material addition. Because material addition by electrodeposition fundamentally arises from atomic-scale behaviors, and the Nano ECAM process operates at an atomic-scale resolution, a corresponding atomic-scale understanding of the process is needed. This work contributes to this objective by using molecular dynamics simulations to study the output migration and deposition of ions in the ECAM process under the influence of varying input electrochemical parameters.

2. Literature review

2.1. Electrodeposition at the nano level

Scaling the ECAM process down to the nano level introduces advantages and considerations that are uniquely distinguished from operation at the macro or micro size scale. Size effects begin to greatly influence the behavior of deposition. For example, a change of interelectrode gap at the micro scale is simply a change in input parameter, with the same fundamental mechanism of deposition occurring [14]. A change in the interelectrode gap at the nano scale can mean the difference between deposition occurring in the quantum tunneling region, the electrical double layer, or bulk electrolyte, which have different structures and behavior [15]. Surface diffusion also begins to play a significant role at the nano scale [16]. Electrochemical nanoscale deposition techniques have relied on modified scanning probe microscopy (SPM) methods, whose nature of operation has provided atomic-scale access for material addition, feedback, and imaging.

Atomic-scale dissimilarities and defects have been used as mechanisms for material addition. Studies have shown the feasibility of mechanical "jump-to-contact" alloying between metal deposited on a scanning tunneling microscope (STM) tip and a dissimilar metal substrate [17]. Another technique has been defect generation by probe scratching [18] or pulsing [19,20] to induce nucleation sites. For ECAM, any reliance on mechanical alloying or defect generation may not be applicable to part build beyond the first layer. Additionally, any mechanical or electrical defect generation may negatively affect the geometrical integrity of the tool and substrate [21].

Direct electrochemical techniques, without prior surface modification, have also been used. Prior studies include ultrashort voltage pulses at double-layer-size interelectrode gaps [22] and local supersaturation-induced deposition [23]. However, these have also used deposition of a dissimilar metal from the original substrate, limiting their applicability to one layer of deposition. For nano scale ECAM, the mechanism of choice is STM-based spot plating of a metal that is homogeneous to the substrate. This technique has been used in micro-scale ECAM extensively [2], and the feasibility of approaching the nano scale using an atomic-scale STM probe has been shown in a prior study for gold-on-gold deposition for one trial using a single set of input parameters [24]. This method suits the voxel-by-voxel material addition inherent to the Nano ECAM process, because it avoids any dependencies on induced defects or interactions between dissimilar metals that would complicate the process. However, the prior work is limited to a single set of input parameters, with the size scale bordering on the micro and nano size regimes. The focus of this study is to use simulation to investigate the performance of the process scaled down to the nano level under varying levels of input parameters. Because this size scale approaches atomic-level resolution, an atomistic approach is needed for simulation; this is further detailed in the next section.

2.2. Atomistic simulations of nano deposition

Electrochemical processes, particularly metal deposition, are incredibly complex and not fully understood at the atomic level. The structure of the electrochemical interface consists of a complex system of differently-charged ions, metal lattices, and solvent [16]. For metal deposition, this involves the drift of randomly-walking ions under an electric field towards the electrode to cross the double layer. Transfer across the double layer then involves simultaneous or sequential chemical bond change, charge transfer, and crystallization processes. These may occur in numerous pathways, depending on the system being studied [16,25–27]. The exact mechanism and sequence of these events is of interest, especially for divalent metal ions, and depending on what species is studied. Different scientists have operated under the theories that ion charge transfer occurs in discrete steps [16,25–29], simultaneously [30], or gradually [29,31–33]. Perspectives also range on whether charge transfer is carried out by an electron jump from the metal to the ion [30], the ion crossing the double layer [29,31,32], or a combination of the two [16,26,27,29,33,34]. Multiple reaction pathways are also possible – for example an ion may directly transfer from the electrolyte to its final deposition spot, or it may transfer to a lower-energy area on the metal surface and then surface diffuse to the final spot [16,26,27,34]. Bulk and surface diffusion are described as stochastic, random-walk processes rather than deterministic ones [25,35].

Due to the complexity and several possible states of electrodeposition at the nanoscale, even for a single ion, the ability to construct a unified and solvable analytical model of the system becomes extremely challenging [21,36]. Further challenges include limitations in the feedback from nanoscale experimental equipment, such as electrochemical scanning tunneling microscopy (ECSTM). The ability to only gather topographical information means the chemical nature of the substrate is not captured, posing limitations in studying alloy deposition. Experiments are also limited in the time scale of scanning and data acquisition, which is in the order of seconds. This means that experiments cannot capture the fine details of interfacial and transport processes that occur at small time scales [37]. Atomistic simulation is a promising approach to study these phenomena at nano scale by allowing greater flexibility with complex configurations than pure theory, and a closer view of electrochemical mechanisms at smaller timescales than can be experimentally captured.

The Nano ECAM process operates on the principle of localized electrochemical deposition on a substrate via a tool of nanoscale geometry. It is therefore essential that the simulation covers the following simultaneously: explicitly-defined nanoscale electrode geometry, constant-potential electrodes, localized charging behavior, and the transition of an aqueous ion to a solid cathode atom under overpotential conditions. The prior work on atomistic simulation overlaps with this study in certain ways, but there is no study which accounts for all elements. Prior work has shown quasi-deterministic [37,38] and stochastic [39] methods to simulate metal deposition, but they have been applied to plating and not localized deposition. Other work simulated localized deposition simulating a burst of ions dissolving from preprogrammed locations on the tool to create localized supersaturation conditions near the surface to drive deposition [40]. However, this mechanism differs from the direct overpotential deposition used in ECAM. Other studies have focused on underpotential deposition, which differs from overpotential deposition [41,42]; as well as the jump-to-contact technique, which is a physical rather than electrochemical process [36,43]. Another study has created a technique of modeling constant-potential electrodes with fluctuating charges to study the adsorption of water between an STM tip and substrate [44]. It has also been studied on ionic liquids [45], but not metal deposition from an aqueous solution. Other studies have gone into finer details of the quantum behavior driving the deposition of a single ion [33,46]. However, simulations involving the quantum level of detail are computationally expensive [47]. This is an issue for the ECAM process, which requires simulating many ions explicitly. This study therefore combines the relevant elements of past studies in a new way, with additional modifications necessary to describe the mechanism of Nano ECAM process.

Different methods of atomic deposition have called for different techniques in simulation [36]. Fully-deterministic molecular dynamics (MD) has been used to model jump-to-contact deposition [43], fully-stochastic Monte Carlo (MC) has been used to study the stability of deposited species using varying techniques [36], and “quasi-deterministic” Langevin dynamics (LD) has been used to study direct electrochemical overpotential deposition [37,38]. In the LD method, implicitly modeling the aqueous solvent allows for a large enough time scale to handle aqueous and solid motion. Most recently, hybrid classical-quantum methods, combining MD with density functional theory (DFT) have been used to model the charge transfer in even finer detail [33].

3. Simulation setup

3.1. Initial conditions

3.1.1. Simulation space

The simulation consists of an anodic tool and cathodic substrate as illustrated in Fig. 1(a). Throughout all trials, the cathode is modeled as a flat plate of a fixed amount atomic layers of copper in the face-centered-cubic arrangement at the bottom of the simulation space. The anode is modeled as a variable-radius hemisphere cut from a platinum FCC lattice block. The space between and surrounding the electrodes is designated as the electrolyte, extending laterally to the borders of the cathode and vertically from the top of the cathode to the top of the anodic hemisphere. This negative space is filled in by “phantom” ions, shown in Fig. 1(b), which are used in subsequent volume and surface area calculations. The matrix of phantom ions follows the extended FCC lattice arrangement of the cathode; as the deposit on the cathode grows, the phantom ions in the corresponding locations switch off.

3.1.2. Aqueous electrolyte

The electrolyte itself is modeled throughout this volume as a fixed amount of randomly-dispersed cation and anion particles as seen in Fig. 1(c). This amount corresponds to an experimental bulk concentration c^0.

The default concentration of copper was chosen to be 1 M, which reflects the copper ion concentration of a 1 M $CuSO_4$ and .5 M H_2SO_4 solution used in a prior experimental paper [19]. However, the nuances of hydrogen and anion behavior were assumed to be outside of the scope of this paper. Instead, a $CuCl_2$ solution was modeled due to the simpler structure of a chloride anion compared to a sulfate anion. The function of the anion in this simulation was primarily to balance out the charge of the cations, but some of the anions were attracted to the substrate and their resulting behavior was similar to selective adsorption and blocking of sites for copper to sit, resembling specific adsorption [48].

Ionic motion is modeled using stochastic Langevin dynamics, representing motion in an implicit aqueous solvent. In addition to the ionic interaction forces $\mathbf{F}_{\text{interaction}}$, which are detailed in the next section, the solvent contributes forces corresponding to friction and random fluctuations, $\mathbf{F}_{\text{frictional}}$ and $\mathbf{F}_{\text{random}}$ as shown in Equation (1) [49]. A further breakdown of velocity-dependent $\mathbf{F}_{\text{frictional}}$ is expressed in Equation (2), where ξ_{fric} is the friction coefficient, r_i is the radius of the ion, η is the viscosity of water, and $\mathbf{v}$ is the instantaneous velocity vector. Equations (3) and (4) detail the stochastic force $\mathbf{F}_{\text{random}}$, for which each x, y, and z component is calculated using a random number from a

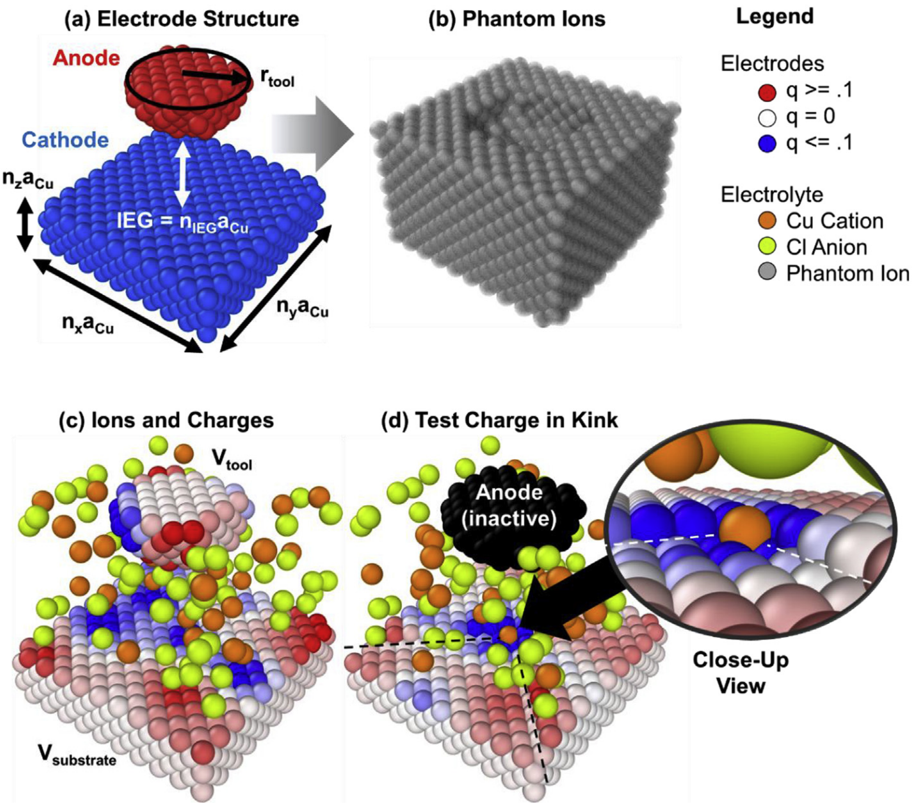

Fig. 1. Simulation domain setup.

Gaussian distribution of mean zero and standard deviation $2m_i k_B T\gamma/\Delta t$, where m_i is the ionic mass, k_B is the Boltzmann constant, T is the temperature, $\gamma = \xi_{fric}/m$ is a coupling constant, and Δt is the simulation timestep [49,50].

$$\mathbf{F}_{net} = \mathbf{F}_{interaction} + \mathbf{F}_{frictional} + \mathbf{F}_{random} \tag{1}$$

$$\mathbf{F}_{frictional} = -\xi_{fric}\mathbf{v} = -6\pi r_i \eta \mathbf{v} \tag{2}$$

$$\mathbf{F}_{random} = [F^{x}_{random},\ F^{y}_{random},\ F^{z}_{random}] \tag{3}$$

$$F^{x,y,z}_{random} = \sqrt{\frac{2m_i k_B T\gamma}{\Delta t}}\,\mathrm{rand}[-1,1] \tag{4}$$

3.1.3. Constant-potential electrodes

The electrode ions, modeled as fluctuating Gaussian charges, are kept at constant user-specified potentials V_{tool} and $V_{substrate}$ throughout the simulation. To hold any solid electrode ion i at a potential V_0 at timestep t, Equation (5) is applied and its charge $q_i(t)$ is solved for [44]. In this equation, the first right-hand term refers to interaction of the Gaussian charge with itself, the second term refers to its interaction with the explicitly-charged cations and anions (indexed by a), and the third term refers to interaction of each charge i with other induced charges $j \neq i$. The parameter $\xi = (1/7)a_i$ corresponds to the width of the Gaussian charges, where a_i is the lattice constant of ion i. Application of this equation to all electrode ions forms a matrix equation which is then solved to obtain all unknown charges q_i.

$$V_0 = \frac{q_i(t)}{\sqrt{\pi}\xi} + \sum_a \frac{q_a \mathrm{erf}\left(\frac{|\boldsymbol{r}_i - \boldsymbol{r}_a|}{\sqrt{2}\xi}\right)}{|\boldsymbol{r}_i - \boldsymbol{r}_a|} + \sum_{j\neq i} \frac{q_j \mathrm{erf}\left(\frac{|\boldsymbol{r}_i - \boldsymbol{r}_j|}{\xi}\right)}{|\boldsymbol{r}_i - \boldsymbol{r}_j|} \tag{5}$$

3.1.4. Interatomic potentials

It was assumed only collisions between the ion and electrode particles were of relevance, except for the discharge and incorporation of the cation into the solid metal cathode lattice under the programmed condition for deposition. Otherwise, the ion was electrostatically repelled from the cathode when it came into contact, representing its location in the Inner Helmholtz Plane [51]. Anion-cathode interaction, such as specific adsorption [48], was not intentionally programmed into or studied by the simulation. However this was captured as a side effect of the few anions that made their way to sites on the substrate by local attraction to their induced image charges. The anions were also repelled electrostatically from the cathode, but their presence blocked the adsorption of copper at the corresponding sites. The tool used in Nano ECAM is an inert Pt-Ir tool. The tool's primary role was to create a localized electric field to drive the motion of the ions. Any reaction at the tool was assumed to be not of interest; therefore any ions contacting the tool would experience repulsion. Finally, only collisions occurred between aqueous ions, which are stably bound in hydration shells in a prepared plating solution [16]. An activation energy is required to pull off the immediate surrounding primary and secondary solvation shells of the aqueous ions, which only happens once the ion transition from the bulk of the solution to the interface [26,27]. This meant that the ions did not interact with one another outside of collisions.

Aqueous cations and anions therefore interacted with each other and the solid copper cathode by a combined Coulomb and truncated "soft-sphere" Lennard-Jones potential [52]. Because it was assumed only collisions between the particles were of relevance, the purely-repulsive truncated Lennard Jones potential was used. It was also assumed that aqueous cations took on the same Lennard Jones parameters as solid copper ions. The Lennard Jones and charge parameters are listed in Table 1. Interaction parameters between unlike particles i and j followed the Lorenz-Berthelot combination rules $\sigma_{ij} = \sigma_{ii}\sigma_{jj}/2$ and $\varepsilon_{ij} = \sqrt{\varepsilon_{ii}\varepsilon_{jj}}$ [53,54].

After a cation was deposited onto the substrate, it would then strictly interact with the surrounding cathode ions via the copper EAM potential [57], an interaction potential for metal lattices, similar to the implementation in prior work [37,38]. Computation of the EAM interaction was done using the open-source LAMMPS molecular dynamics software [58]. All anode ions were assumed to remain inert and unmoving.

Table 1
Ionic interaction potentials.

Ion	σ (Å)	ε $(kcal/mol)$	q	Reference
Cu^{2+}	2.616	4.72	2	[55]
Cl^{-}	4.40	.1	−1	[56]

3.2. Boundary conditions

3.2.1. Mechanism of deposition

According to fundamental literature [51], overpotential deposition occurs in four main steps: (1) diffusion of the ion from the bulk to the double layer; (2) charge transfer of the ion across the double layer; (3) chemical reactions associated with the depositing ion; and (4) crystallization via surface diffusion of the deposited ions. Steps (1) and (2) were modeled by the ionic motion under the influence of the stochastic Langevin forces and drift under the electric field of the electrodes. When a cation reaches within a_{Cu} of any solid cathode atom, steps (3) and (4) were implemented as follows.

Prior literature modeled plating on a substrate under varying overpotentials by using a constant background chemical potential parameter μ representing the electrode overpotential $\eta = -(1/ze_0)(\mu - \mu_0)$. An ion near the electrode would gradually begin to experience of the EAM potential U_{EAM} from the electrode lattice. When the condition $U_{EAM} < \mu$ was met, the ion transitioned from aqueous to solid [37,38]. In this study, there was no explicit or localized counter electrode that was modeled; instead, the resulting substrate overpotential was implicit in the value of μ.

In contrast to the study of plating, simulation of localized nanoscale deposition must explicitly handle the atomic-scale geometry, placement, and charge distribution of a nanoscale tool counter electrode. This results in a dynamic electrochemical environment in the surrounding electrolyte across space and time that cannot be captured by a constant parameter. Therefore, the constant background potential method was extended to a dynamic background potential which could track the changing potential experienced by each aqueous cation across space and time. When each cation reached the interface, this value was used to evaluate the whether the transfer of ion from solution to substrate would occur, depending on the electrochemical potential experienced by the ion. The dynamic monitoring of μ was implemented by linking to another definition of overpotential in terms of electrostatic potential differences, $\eta = \Delta\varphi - \Delta\varphi_0$, as seen in Equation (6) [51]. Terms with the subscript $_0$ denote when a deposited ion in a kink is at equilibrium at a given substrate potential and concentration. This "test kink" condition is illustrated in Fig. 1(d). The electrostatic potential φ_0^S experienced by the test ion i by all other ion and electrode charges j as it sits in the kink shown in the figure, where $\varphi_0^S = \sum_{j\neq i}(kq_j/r_{ij})$. The reference chemical potential μ_0 is the potential energy of the kink ion interaction with the rest of the cathode lattice via the EAM potential.

Terms without the subscript $_0$ denote dynamic variables monitored during deposition. The potential difference $\Delta\varphi$ is equal to the difference in potential between metal and solution $\varphi^M - \varphi^S$ [51], and the equation is further expanded into Equation (7). Because in both the test kink and simulation cases the substrate potential within the metal is identical, the φ^M terms cancel out as seen in Equation (8). Finally, Equation (9) shows the equation rearranged to give a dynamic value of μ that depends on the variable electrostatic potential φ^S experienced by an ion i by all other ion and electrode charges j as it moves around the system, where $\varphi^S = \sum_{j\neq i}(kq_j/r_{ij})$. This dynamic μ value is evaluated against

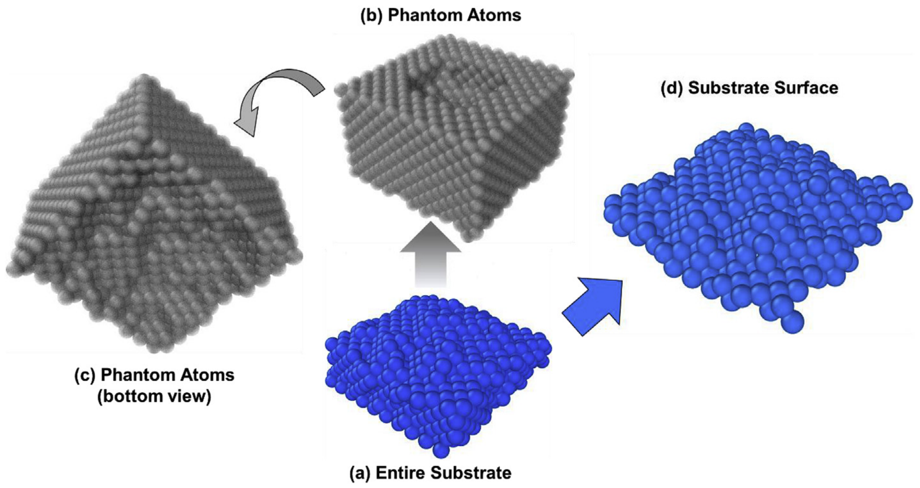

Fig. 2. As the deposition progresses, the following changes are monitored: (a) atoms making up the total volume of the substrate and deposit, (b,c) imaginary "phantom" ions representing the electrolyte volume, and (d) atoms on the surface of the substrate exposed to the electrolyte (used for surface area and current density calculations).

U_{EAM} when the ion nears the substrate surface.

$$\Delta\varphi - \Delta\varphi_0 = -\frac{1}{ze_0}(\mu - \mu_0) \tag{6}$$

$$(\varphi^M - \varphi^S) - (\varphi_0^M - \varphi_0^S) = -\frac{1}{ze_0}(\mu - \mu_0) \tag{7}$$

$$\varphi_0^S - \varphi^S = -\frac{1}{ze_0}(\mu - \mu_0) \tag{8}$$

$$\mu = \mu_0 - ze_0(\varphi_0^S - \varphi^S) \tag{9}$$

3.2.2. *Maintaining constant concentration*

As described previously, the charges fluctuate on the electrodes to maintain their constant potential condition, and when the cations reach the cathode, they undergo the potential checking procedure for metal deposition. As a result, the boundary of the substrate grows as seen in Fig. 2(a) and the boundary of the phantom atoms shrinks over time, shown in Fig. 2(b) and (c). The phantom ion lattice was updated by "switching off" any phantom ions that were within a distance of $a_{Cu}/2$ of any solid substrate ions. This was then used to approximate volume changes over time in order to maintain a constant concentration. With a flat substrate, the initial volume was $V_0 = a_{Cu}n_x a_{Cu}n_y(a_{Cu}/2)n_z$ with a phantom ion count of P_0. As the phantom ion count changed to $P(t)$, the volume $V(t)$ was updated using Equation (10).

$$V(t) \approx \frac{P(t)}{P_0}V_0 \tag{10}$$

The bulk concentration was calculated from the initial number of atoms n_0 and initial electrolyte region volume V_0, giving a concentration value of $c_0 = n_0/V_0$. The number of atoms throughout the simulation $n(t)$ was adjusted as shown in Equation (11) to maintain a constant concentration.

$$n(t) \sim c_0V(t) \tag{11}$$

3.2.3. *Incoming ionic flux*

If a deposition resulted in the electrolyte volume reducing such that the remaining ions $n'(t)$ were less than the calculated $n(t)$, then $n(t) - n'(t)$ atoms were added back into the systems as a flux into the side walls to maintain constant concentration. It was assumed that the flux into the side walls J_{in} was equal to the outward flux due to consumption of ions J_{out}. This outbound flux J_{out} was calculated as shown in Equation (12) based on the number of ions that deposit on area $A(t)$ during a single timestep [35].

$$J_{out} = \frac{(n(t) - n'(t))}{A(t)\Delta t} \tag{12}$$

The position along the side wall was generated randomly, and the incoming velocity was calculated using the relation between velocity, flux, and concentration [35], as seen in Equation (13).

$$v_{in} = \frac{J_{in}}{c_0} = \left(\frac{1}{c_0}\right)\frac{(n(t) - n'(t))}{A\Delta t} \tag{13}$$

In order to determine the substrate surface area, the substrate surface atoms that were exposed to the electrolyte were first detected. This was done by finding the number of phantom ion nearest neighbors P_i' corresponding to each substrate ion i, which was detected if the phantom ion was located within $.9a_{Cu}$ of the solid ion. If $P_i' > 0$, then ion i was considered a substrate surface ion. An example image of detected surface ions is shown in Fig. 2(d). For each surface ion, its contribution to the deposit surface area was approximated as shown in Equation (14) at each timestep by multiplying P_i' by 1/12th of the ionic sphere's surface area, $4\pi r_{Cu}^2$. The ionic radius r_{Cu} was equal to .73 Å [59].

$$A(t) = \frac{4\pi r_{Cu}^2}{12}\sum P'_i(t) \tag{14}$$

The scope of this simulation study focused on deposition by electrochemical transport of ions away from the anode and towards the cathode, which is associated with faradaic current. However, when the gap shrinks to a sufficient distance, electron tunneling begins to occur, which is a completely different mechanism outside the scope of this study. Therefore, tunneling is avoided and each run was set to terminate when the interelectrode gap shrank to the electron tunneling distance, which occurs when the tip is so close to the surface that the electronic wave functions overlap. In the simulation, this is assumed to be $1.5a_{cu} \sim 4$Å. Tunneling is an entirely different type of current flow than faradaic. When the tunneling starts, there is no chemical change and therefore no deposition. Additionally, this choice of termination criteria is linked to experiment, where a current spike the tip-surface tunneling current is the sign that an STM tip is near the substrate [60].

3.3. *Input parameters*

The input parameters studied were the tool size, tool potential, substrate potential, interelectrode gap, and electrolyte concentration. The default condition was a tool radius of 10 Å, tool voltage of 3 V, substrate voltage of .340 V, interelectrode gap of 5a$_{Cu}$, and electrolyte concentration of 1.5 M. The tool radius was varied to 5, 10, and 20 Å; the tool voltage was varied to 2 and 5 V; the substrate voltage was varied to 0 and .340 V; the interelectrode gap was varied to 3a$_{Cu}$ and 10a$_{Cu}$; and the concentration was varied to .5, 1.0, and 2.0 M.

Simulations were run until an interelectrode gap between any atom on the anode and grown deposit shrunk below the 4 Å tunneling limit, or the simulation time exceeded 35 days.

3.4. Output parameters

The output parameters monitored at each timestep t included following geometrical and electrochemical behavior over time:

- Deposit height $h(t)$, extracted from the simulation
- Number of atoms deposited $D(t)$, extracted from the simulation
- Averaged current density $j_{avg}(t)$ was calculated using Equation (15) each time an ion was deposited. In this equation, z is the valence of the copper ions, e_0 is the elementary charge, $A(t)$ is the approximated surface area of the growing cathode exposed to the electrolyte, t_D is the integer amount of timesteps that have passed since the last ion deposited, and Δt is the simulation timestep.

$$j_{avg}(t) = ze_0\frac{D(t)}{A(t)t_D\Delta t} \tag{15}$$

- Quality factor 1, Q_1, was used to evaluate the geometrical integrity of the deposit as a convex-shaped voxel. Q_1 was expressed as a ratio of the non-plated height $h_t - h_p$ to the total deposit height h_t, where h_p was defined as the plating height. The plating atoms of the deposit were classified as any atom whose radial distance from beneath the tool center was over 80% of the maximum deposit radius. The plating height h_p was the maximum height extracted from the set of atoms classified as part of the plating region. This factor was designed such that a dome-like deposit shape would give higher Q_1 values, and a flat deposit would give lower Q_1 values.

$$Q_1 = \frac{h_t - h_p}{h_t} \tag{16}$$

- Quality factor 2, Q_2, was designed to capture the change of the deposit's volume-to-surface area ratio, relative to the beginning ratio corresponding to the flat substrate. This factor was also designed to result in a higher value for dome-like deposits and a lower value for flat deposits.

$$Q_2 = \frac{\left(\frac{V}{A}\right) - \left(\frac{V}{A}\right)_{initial}}{\frac{V}{A}_{initial}} \tag{17}$$

4. Results and discussion

4.1. Effect of tool size

The influence of the tool size on the nano electrodeposition process is shown in Fig. 3. The reduction of tool size results in an overall faster-growing deposit. This is also correlated with current density, which increases with reduction of tool size. However, the final output geometry shows that the smallest tool actually gives the worst-quality deposit; instead of the intended convex voxel shape, a concave shape grew around the tool without any atoms near enough to the tool to register tunneling.

The quality of deposition, seen qualitatively in the geometrical plots, is reflected in the areas under the curves in the Q_1 plot (plating height ratio), where the best-quality deposits had the highest areas. However, the Q_1 value appears to follow fluctuating stepwise behavior throughout the deposition. The final values seen in the Q_1 plot do not reflect the final quality of the deposit. The trend seen in the final values in the Q_2 plot (volume-to-surface-area ratio) overall agrees with the final shape of the deposits seen in the geometrical plots, except for the smallest tool. This shows that the final volume-to-surface-area ratio gives some useful insight into evaluating the final quality of the deposit. However, this ratio alone cannot be used as a quality factor, because it cannot capture the nature of a concave deposit forming. Therefore, both quality factors can be used to evaluate the deposit. Overall, it was seen that at this fixed interelectrode gap $5a_{Cu}$, there is an optimal radius value of 1.5 Å that gives the best quality of deposition. Any increase in radius results in a decrease in quality, likely due to a wider distribution of the electric field and a sparser charge density distributed throughout the electrode. Any decrease in radius also resulted in a decrease in quality, likely explained by less atoms present to exert an electrostatic force on the cations, even though the smallest tool would have had the strongest induced charges and electric field per atom.

4.2. Effect of tool and substrate voltage

Tool voltage, as seen in Fig. 4, appeared to have a direct relationship to the initial deposition speed and initial current density. However, the final current densities followed an inverse relationship. This is likely due to the more rapid ion depletion resulting from a higher potential difference.

The deposition qualities seen in the geometrical plots also appear to increase with tool voltage. This is reflected in the areas under the curves in the plating height ratio plot. However, the volume-to-surface area ratio change plot deviated from this relationship, with the highest-voltage tool appearing to have the worst performance. Upon closer inspection of the geometrical plot for the 5 V condition, the deposit appears to have a hollow center that would increase the surface area and drive the ratio lower. This hollow center is likely a result of the rapid depletion of ions beneath the center of the tool at the high voltage. Overall, this shows that an increase in voltage results in a taller, faster, and higher quality deposit for the larger-scale shape of the deposit, but increasing tool voltage past a certain point introduces hollowness within the deposition.

As seen in Fig. 5, the substrate voltage changes were more subtle than those of the tool voltages, based on values from literature for nanoscale copper deposition [22]. The deposition rate and current density were all close to each other in value throughout the runs. However, the lowest substrate voltage (0 V) exhibited a faster ion depletion rate than the others, as seen in the falling edge of the current density plot. This coincided with a hollow area in the middle of the deposit, as seen in the geometrical plot. The first quality factor also appeared highest for the 0 V deposit, as seen in the slightly higher area under its curve. This deposit also performed the best in the second quality factor plot, with the highest final value. The .740 V deposit performed second-best due to its symmetrical and overall convex shape. The .340 V deposit had a sharp protrusion, but it was surrounded by a larger plating area, which was likely the reason for the lowest final value of the second quality factor. Overall, it appears that the lowest substrate voltage had the same effect as the highest tool voltage, likely due to both factors affecting the overall potential difference between the electrodes. However, above this point, the behavior is more arbitrary and may be a result of complex interactions between a weaker potential difference, cations, and anions.

4.3. Effect of interelectrode gap

Fig. 6 shows that the shortest interelectrode gap gave the fastest deposition and rapid, tall spike in current density. However, this was short-lived and a maximum height corresponding to two atomic layers was deposited until tunneling was detected. The highest quality deposit was the middle interelectrode gap, as evident in both quality factor plots and the geometric plots. A further increase in height resulted in a slower deposition, lower current density, and lower quality. Overall, it is evident that for this given tool radius, an optimal interelectrode gap that balances current density and quality exists. This is important, because the typical feedback during an experiment is limited to current

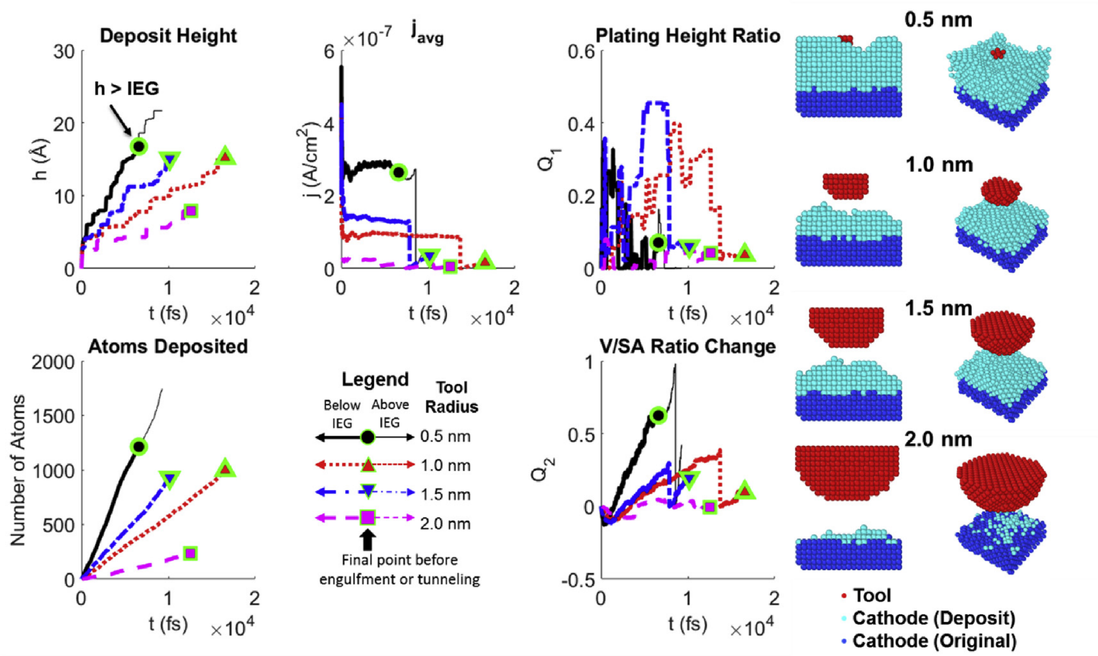

Fig. 3. Influence of tool radius on output parameters.

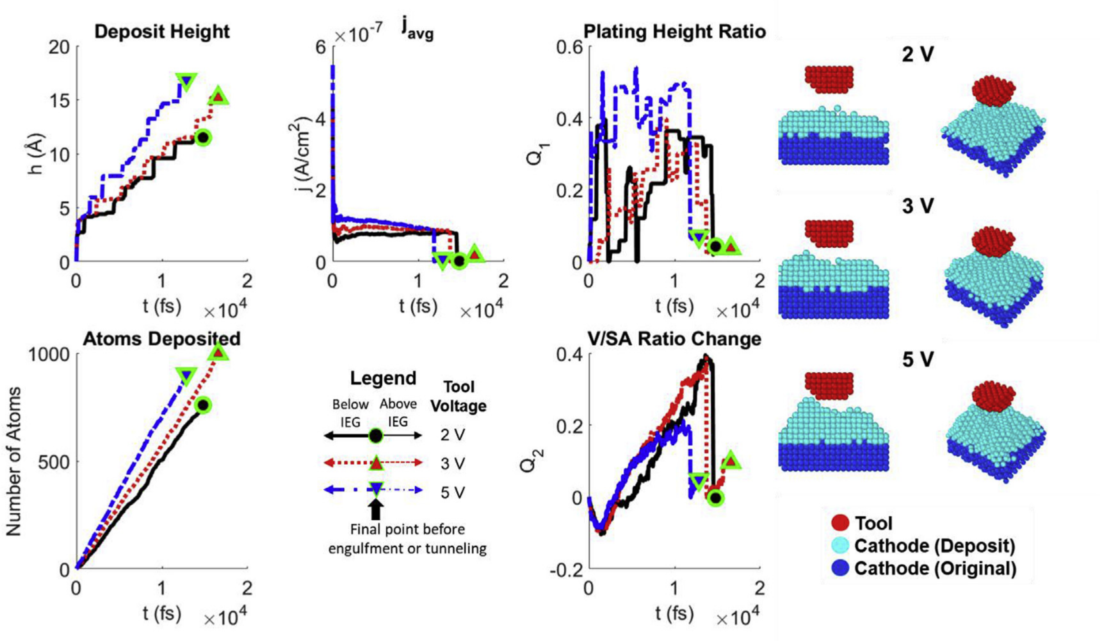

Fig. 4. Influence of tool voltage on output parameters.

density. However, unlike with the prior parameters, the current density is not correlated with the final quality of the deposit. This shows that the interelectrode gap has the most influence on changing the in-situ electrical behavior, final output geometry, and the nature of the relationship between the two.

4.4. Effect of ion concentration

Fig. 7 shows that the deposition speed and current density were lowest for the extreme (highest or lowest) concentration values, and these output parameters were highest for the middle concentration values. However, similar to the interelectrode gap trials, the deposition quality did not completely correlate with deposition speed and current density. The highest concentration of electrolyte gave the highest quality deposit, reflected in both quality plots and the geometrical plot, despite having the slowest deposition speed and lowest output current density. This is likely due to the increased resistance to diffusion as more aqueous species cause more collisions with each other. The lowest concentration gave the slowest deposition rate and lowest current density due to less ions being present to deposit. This resulted in the worst-quality deposition that grew around the tool, similar to the trial with the smallest tool size. A commonality between these two trials is that there are less overall anode-cation pair interactions, likely resulting in the overall electrolyte not diffusing away from the tool was fast. The plating height ratio plot overall corresponds to the geometrical plots, while the volume-to-surface-area plot holds some deviations. Overall, it

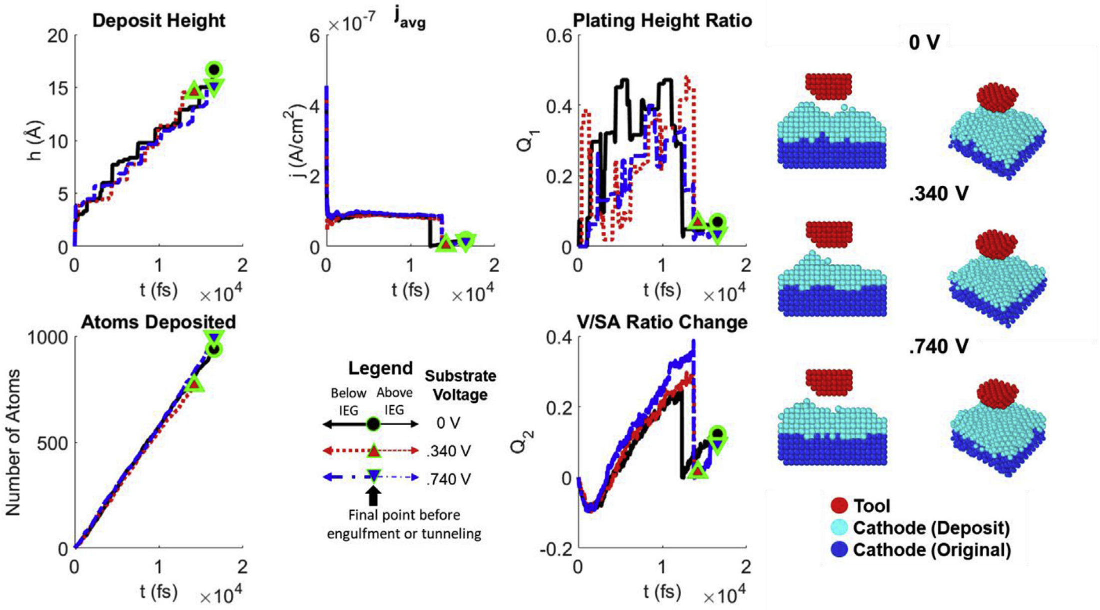

Fig. 5. Influence of substrate voltage on output parameters.

can be seen that if quality is the priority, then the higher 2.0 M electrolyte is the desired choice. If deposition speed is the priority, then a moderate 1.0–1.5 M electrolyte concentration should be selected. Any lower concentrations result in a decrease in both deposition speed and quality.

5. Conclusions

A quasi-deterministic molecular dynamics simulation was performed to study the migration and deposition of ions under the influence of charged, constant-potential electrodes. Deposition quality was evaluated quantitatively using two different quantitative approaches, as well as qualitative evaluation of the output geometry. It was found that at the given interelectrode gap studied, there was an optimal radius for maximum deposition speed and quality. Similarly, there was an optimal interelectrode gap at the radius studied for deposition quality, but the relationship with speed deviated. It was seen that varying the interelectrode gap and concentration allowed for inverse control over the deposition speed and quality – as deposition speed increased, quality decreased; and vice-versa. Variation of tool and substrate voltage gave a coupled change in deposition speed and quality, where both would simultaneously increase or decrease. Overall, with some exceptions, a higher tool-substrate voltage difference resulted in higher deposition speed and quality. Ion depletion behavior was seen in the runs with the highest voltage differentials and the lowest concentration, resulting in a hollow feature in the center of the deposit. Another pattern seen was that the overall lower amount of anode-cation pairs due to a lower tool size or concentration led to an overall weaker drift of the ions to a

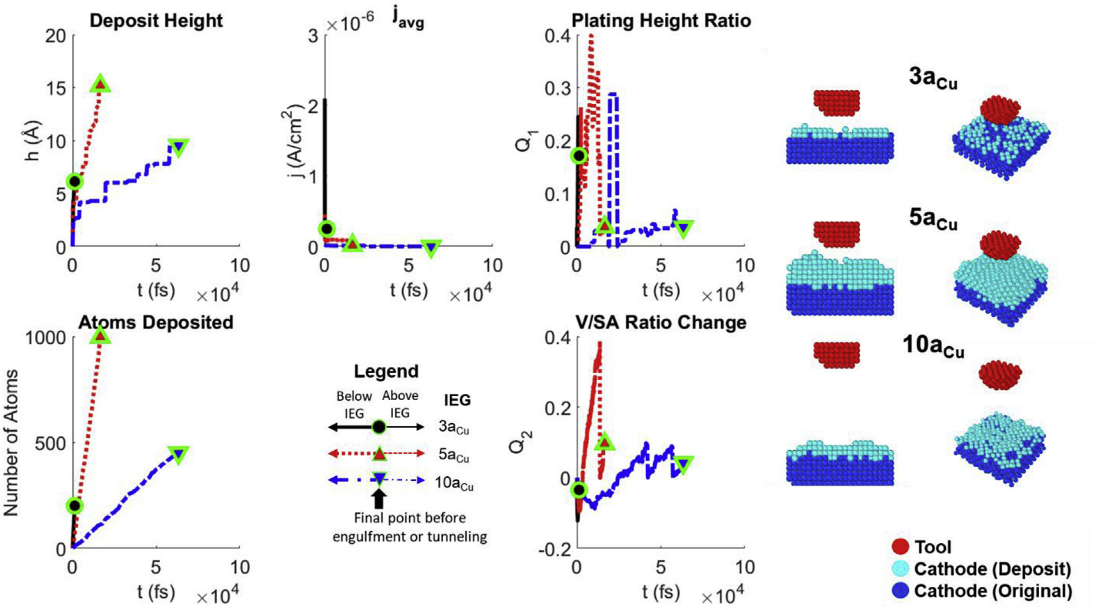

Fig. 6. Influence of interelectrode gap (IEG) on output parameters.

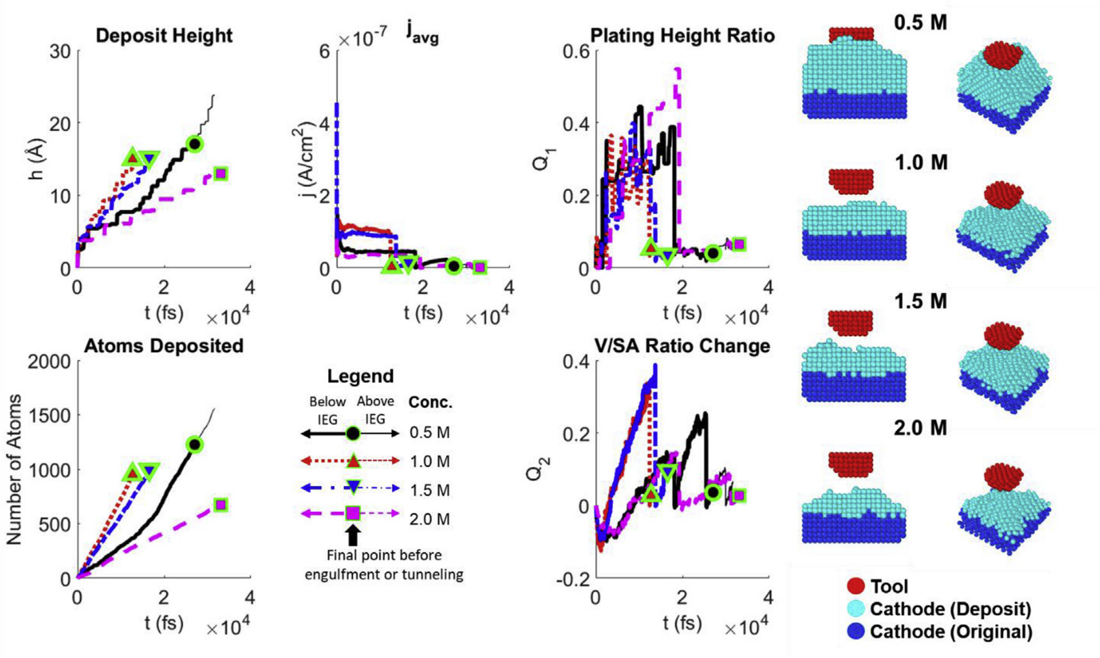

Fig. 7. Influence of electrolyte concentration on output parameters.

localized spot on the substrate, instead resulting in substrate growth engulfing the tool. Overall, this study shows how input electrochemical parameters influence the output deposition speed and geometry in spot plating for nanoscale electrochemical additive manufacturing. The current density calculated from the tool tip size and current, which is typically the feedback signal monitored in experiments, was seen to not necessarily be a direct reflection of the deposition geometry.

Acknowledgments

This material is based upon work supported by the National Science Foundation under Grant No. CMMI-1454181. Any opinions, findings, and conclusions or recommendations expressed in this material are those of the author(s) and do not necessarily reflect the views of the National Science Foundation. High-performance computing resources were provided by the UC Mechanical and Materials Engineering Department.

Appendix A. Supplementary data

Supplementary data to this article can be found online at https://doi.org/10.1016/j.precisioneng.2019.01.010.

References

[1] Said RA. Localized electro-deposition (LED): the march toward process development. Nanotechnology 2004;15:S649.
[2] Sundaram MM, Kamaraj AB, Kumar VS. Mask-less electrochemical additive manufacturing: a feasibility study. J Manuf Sci Eng 2015;137:021006.
[3] Brant A, Sundaram MM. A novel system for cloud-based micro additive manufacturing of metal structures. J Manuf Process 2015;20:478–84.
[4] Said RJN. Microfabrication by localized electrochemical deposition: experimental investigation and theoretical modelling. 2003;14:523.
[5] Madden JD, Hunter IWJJoms. Three-dimensional microfabrication by localized electrochemical deposition. 1996;5:24–32.
[6] Gibson I, Rosen DW, Stucker B. Additive manufacturing technologies. Springer; 2010.
[7] Vaezi M, Seitz H, Yang S. A review on 3D micro-additive manufacturing technologies. Int J Adv Manuf Technol 2013;67:1721–54.
[8] Ullett JS, Benson-Tolle T, Schultz JW, Chartoff R. Thermal-expansion and fracture toughness properties of parts made from liquid crystal stereolithography resins. Mater Des 1999;20:91–7.
[9] Kumar VS, Sundaram MM. Experimental study of binding copper powders by electrochemical deposition. Proc IME B J Eng Manufact 2017;231:1309–18.
[10] Chen H, Zhao YF. Process parameters optimization for improving surface quality and manufacturing accuracy of binder jetting additive manufacturing process. Rapid Prototyp J 2016;22:527–38.
[11] Gao W, Zhang Y, Ramanujan D, Ramani K, Chen Y, Williams CB, et al. The status, challenges, and future of additive manufacturing in engineering. Comput Aided Des 2015;69:65–89.
[12] Meteyer S, Xu X, Perry N, Zhao YF. Energy and material flow analysis of binder-jetting additive manufacturing processes. Procedia CIRP 2014;15:19–25.
[13] Brant A, Sundaram M. A novel electrochemical micro additive manufacturing method of overhanging metal parts without reliance on support structures. Procedia Manufacturing 2016;5:928–43.
[14] Kamaraj AB, Sundaram M. A study on the effect of inter-electrode gap and pulse voltage on current density in electrochemical additive manufacturing. J Appl Electrochem 2018;48:463–9.
[15] Brant AM, Sundaram M. A fundamental study of nano electrodeposition using a combined molecular dynamics and quantum mechanical electron force field approach. Procedia Manufacturing 2017;10:253–64.
[16] Bockris JOM, Reddy AK. Electrodics. Volume 2 modern electrochemistry. Springer; 1970. p. 845–990.
[17] Kolb D, Ullmann R, Ziegler J. Electrochemical nanostructuring. Electrochim Acta 1998;43:2751–60.
[18] LaGraff JR, Gewirth AA. Enhanced electrochemical deposition with an atomic force microscope. J Phys Chem 1994;98:11246–50.
[19] Xia X, Schuster R, Kirchner V, Ertl G. The growth of size-determined Cu clusters in nanometer holes on Au (111) due to a balance between surface and electrochemical energy1. J Electroanal Chem 1999;461:102–9.
[20] Li W, Hsiao G, Harris D, Nyffenegger R, Virtanen J, Penner R. Mechanistic study of silver nanoparticle deposition directed with the tip of a scanning tunneling microscope in an electrolytic environment. J Phys Chem 1996;100:20103–13.
[21] Leiva E, Schmickler W. Theories and simulations for electrochemical nanostructures. Electrochemistry at the nanoscale. Springer; 2009. p. 1–31.
[22] Schuster R, Kirchner V, Xia X, Bittner A, Ertl G. Nanoscale electrochemistry. Phys Rev Lett 1998;80:5599.
[23] Hofmann D, Schindler W, Kirschner J. Electrodeposition of nanoscale magnetic structures. Appl Phys Lett 1998;73:3279–81.
[24] Schneir J, Hansma P, Elings V, Gurley J, Wickramasinghe K, Sonnenfeld R. Creating and observing surface features with a scanning tunneling microscope. Scanning Microscopy Technologies and Applications. International Society for Optics and Photonics; 1988. p. 16–22.
[25] Bockris JOM, Razumney GA. Fundamental aspects of electrocrystallization. 1967.
[26] Conway B, Bockris JM. On the calculation of potential energy profile diagrams for processes in electrolytic metal deposition. Electrochim Acta 1961;3:340–66.
[27] Conway BE, Bockris JM. The mechanism of electrolytic metal deposition. Proc Roy Soc Lond A 1958;248:394–403.
[28] Anderson JL, Shain I. Cyclic voltammetric studies of the pH dependence of copper (II) reduction in acidic aqueous nitrate and perchlorate solutions. Anal Chem 1976;48:1274–82.
[29] Gileadi E. Charge and mass transfer across the metal/solution interface. Isr J Chem 2008;48:121–31.
[30] Gileadi E. Simultaneous two-electron transfer in electrode kinetics. J Electroanal

Chem 2002;532:181–9.
[31] Gileadi E. The enigma of metal deposition. J Electroanal Chem 2011;660:247–53.
[32] Gileadi E. Can an electrode reaction occur without electron transfer across the metal/solution interface? Chem Phys Lett 2004;393:421–4.
[33] Pinto L, Quaino P, Santos E, Schmickler W. On the electrochemical deposition and dissolution of divalent metal ions. ChemPhysChem 2014;15:132–8.
[34] BJ O'M, Razumney G. Fundamental aspects of electrocrystallisation. New York: Plenum; 1967.
[35] Bockris JOM, Reddy AK. Ion transport in solutions. Modern electrochemistry. Springer; 1970. p. 287–460.
[36] Staikov GT. Electrocrystallization in nanotechnology. John Wiley & Sons; 2007.
[37] Mariscal M, Leiva E, Pötting K, Schmickler W. The structure of electrodeposits–a computer simulation study. Appl Phys A 2007;87:385–9.
[38] Schmickler W, Pötting K, Mariscal M. A new simulation model for electrochemical metal deposition. Chem Phys 2006;320:149–54.
[39] Pricer TJ, Kushner MJ, Alkire RCJJotES. Monte Carlo simulation of the electrodeposition of copper I. Additive-free acidic sulfate solution 2002;149:C396–405.
[40] Mariscal MM, Leiva EP, Dassie SAJJoEC. Computer simulation of electrochemical nanostructuring induced by supersaturation conditions. 2007;607:10–6.
[41] Oviedo O, Negre C, Mariscal M, Sánchez C, Leiva EJEC. Underpotential deposition on free nanoparticles: its meaning and measurement. 2012;16:1–5.
[42] Gimenez MC, Del Popolo MG, EPJEa Leiva. Monte Carlo simulation for the formation and growth of low dimensionality phases during underpotential deposition of Ag on Au (100). 1999;45:699–712.
[43] Landman U, Luedtke W, Burnham NA, Colton RJ. Atomistic mechanisms and dynamics of adhesion, nanoindentation, and fracture. Science 1990;248:454–61.
[44] Siepmann JI, Sprik M. Influence of surface topology and electrostatic potential on water/electrode systems. J Chem Phys 1995;102:511–24.
[45] Merlet C, Rotenberg B, Madden PA, Salanne M. Computer simulations of ionic liquids at electrochemical interfaces. 2013;15:15781–92.
[46] Pinto LM, Spohr E, Quaino P, Santos E, Schmickler W. Why silver deposition is so fast: solving the enigma of metal deposition. 2013;52:7883–5.
[47] Taylor CD, Marcus P. Molecular modeling of corrosion processes: scientific development and engineering applications. John Wiley & Sons; 2015.
[48] Despić AR. Deposition and dissolution of metals and alloys. Part B: mechanisms, kinetics, texture, and morphology. Comprehensive treatise of electrochemistry. Springer; 1983. p. 451–528.
[49] Leach AR. Molecular modelling: principles and applications. Pearson education; 2001.
[50] Phillips CL, Anderson JA, Glotzer SC. Pseudo-random number generation for brownian dynamics and dissipative particle dynamics simulations on GPU devices. J Comput Phys 2011;230:7191–201.
[51] Paunovic M, Schlesinger M. Fundamentals of electrochemical deposition. john wiley & sons; 2006.
[52] Rapaport DC, Rapaport DCR. The art of molecular dynamics simulation. Cambridge university press; 2004.
[53] Lorentz H. Ueber die Anwendung des Satzes vom Virial in der kinetischen Theorie der Gase. Ann Phys 1881;248:127–36.
[54] Berthelot D. Sur le mélange des gaz. Compt Rendus 1898;126:1703–6.
[55] Heinz H, Vaia R, Farmer B, Naik R. Accurate simulation of surfaces and interfaces of face-centered cubic metals using 12− 6 and 9− 6 Lennard-Jones potentials. J Phys Chem C 2008;112:17281–90.
[56] Chandra A. Dynamical behavior of Anion− water and Water− water hydrogen bonds in aqueous electrolyte solutions: a molecular dynamics study. J Phys Chem B 2003;107:3899–906.
[57] Foiles S, Baskes M, Daw MS. Embedded-atom-method functions for the fcc metals Cu, Ag, Au, Ni, Pd, Pt, and their alloys. Phys Rev B 1986;33:7983.
[58] Plimpton S. Fast parallel algorithms for short-range molecular dynamics. J Comput Phys 1995;117:1–19.
[59] Shannon RD. Revised effective ionic radii and systematic studies of interatomic distances in halides and chalcogenides. Acta Crystallogr - Sect A Cryst Phys Diffr Theor Gen Crystallogr 1976;32:751–67.
[60] Bard AJ, Faulkner LR, Leddy J, Zoski CG. Electrochemical methods: fundamentals and applications. New York: wiley; 1980.